Electronic Supplementary Material (ESI) for Journal of Materials Chemistry C.

Achieving low-consumption bio-based piezoelectric nanogenerator *via* modulating inner layer thickness for highly sensitive pedometer

Zixiong Sun[a,b,c,d,e], Siting Wang[a], Shibo Zhao[a], Hansong Wei[b], Guodong Shen[f*], Yongping Pu[g], Sufeng Zhang[b*]*

a School of Electronic Information and Artificial Intelligence, Shaanxi University of Science and Technology, Xi'an 710021, PR China

b Shaanxi Provincial Key Laboratory of Papermaking Technology and Specialty Paper Development, National Demonstration Center for Experimental Light Chemistry Engineering Education, Key Laboratory of Paper Based Functional Materials of China National Light Industry, Shaanxi University of Science and Technology, Xi'an, 710021, PR China

c Key Laboratory of Auxiliary Chemistry and Technology for Chemical Industry, Ministry of Education, Shaanxi University of Science and Technology, Xi'an 710021, PR China

d Shaanxi Collaborative Innovation Center of Industrial Auxiliary Chemistry and Technology, Shaanxi University of Science and Technology, Xi'an 710021, China

e MESA$^+$ Institute for Nanotechnology, University of Twente PO Box 217, 7522 NH Enschede, The Netherlands

f School of Textile Science and Engineering, Xi'an Polytechnic University

g School of Materials Science and Engineering, Shaanxi University of Science and Technology, Xi'an 710021, PR China

**Corresponding author: Zixiong Sun, Guodong Shen, Sufeng Zhang*

E-mail address: SunZX@sust.edu.cn, shenguodong@xpu.edu.cn, zhangsufeng@sust.edu.cn

Supplementary Information

Experimental Section

Materials and reagents

Fig. S1 sketches the experimental technology for fabricating the *CP*-BCZT PENGs in this work. Cellulose was purchased from Hubei Jinhuan New Material Technology *Co., Ltd*. The DMAc (99.0%), LiCl (99.0%), PVDF (average Mw~534,000 $gmol^{-1}$), barium chloride ($BaCl2\cdot2(H_2O$), 99.0%), calcium chloride ($CaCl_2$, 99.0%), zirconium oxychloride octahydrate ($ZrOCl2\cdot8(H_2O)$, 99.0%), and the titanium tetrachloride ($TiCl_4$, 99.0%) were all purchased from Sinopharm Chemical Reagents *Co., Ltd*.

Preparation of BCZT fillers by hydrothermal method

$Ba_{0.3}Ca_{0.7}Zr_{0.2}Ti_{0.8}O_3$ (BCZT) inorganic nano-ceramic fillers were prepared through the hydrothermal method, with the raw materials of $BaCl_2\cdot2H_2O$, $CaCl_2$, $ZrOCl_2\cdot8H_2O$, and $TiCl_4$. First, the $BaCl_2\cdot2H_2O$, $CaCl_2$, and $ZrOCl_2\cdot8H_2O$ were added into deionized water separately, and the solutions were stirred at room temperature until the powders were completely dissolved. Then, mixed them and added $TiCl_4$ dropwise until completely dissolved. This process can be done in frozen-water circumstances to prevent the HCl(g)'s volatilization. The precursor of BCZT was then obtained by adding proper quality NaOH(*s*) with severe reactions. After a standing of ~10 min, the obtained BCZT precursor was transferred to the hydrothermal reactors, and a hydrothermal reaction was carried out at 200 ^oC for 12 h. When the reactions finished, the powders were transferred to 2L beakers full of deionized water and started a washing process with the repetition of over five times to remove the Cl^{-1}. After this, the powder can be obtained after drying at 80 ^oC for 24 h.

Preparation of the cellulose/PVDF-BCZT precursor

The manufacturing process of cellulose/PVDF-BCZT (*CP*-BCZT) precursors follows the techniques of our previous work[1]. In brief, the transparent cellulose solution dissolved by DMAc and the PVDF dissolved by DMAc were mixed according to the mass ratio 4:1 to get the RC/PVDF mixture. Then, the as-prepared BCZT particles obtained from the hydrothermal method mentioned above were added with a volume fraction of 2% of the *CP* blend precursor, which was obtained by using its mass to divide its density (~5.57 g/cm^3). The ternary solution doped with two different BZT and BST fillers should be stirred for at least 12 hours until evenly mixed. Finally, the precursors RC/PVDF-BCZT films were obtained by ultrasonic oscillation-assisted magnetic stirring for 30 minutes, repeated six times.

Preparation of the cellulose/PVDF-BCZT sandwich structured films

Sandwich-structured *CP*-BCZT films were prepared by casting method. Unlike traditional techniques, in our work, to make the interaction between adjacent layers more active through hydrogen bonding, each layer of the three-layer structure is cast before the previous layer is completely dry. The outer layers of the sandwich-structured films are cast with pristine *CP* solution, and the middle layer is cast with *CP*-BCZT ternary solution. Keeping the total thickness the same changes the inner layer thickness to *1/5*, *1/3,* and *3/5* of the total thickness, and the corresponding configurations are written as *0-1/5-0*, *0-1/3-0*, and *0-1/5-0*, respectively. A configuration of 0-0-0 without BCZT fillers' embedding was also fabricated for a control experiment.

Preparation of the cellulose/PVDF-BCZT piezoelectric nanogenerators (PENGs)

Cut a circular piece (size: 3 cm in diameter) from the as-prepared films mentioned above,

and cut two circular copper electrodes (length: 2.8cm in diameter) of the same size and attach them to the upper and lower surfaces of the composite film. The main agent and curing agent of the encapsulating material polydimethylsiloxane (PDMS) are mixed evenly in a ratio of 10:1 and placed in a vacuum-drying box to remove bubbles in the mixed solution. Place the film attached to the electrode in a container. The mixed solution with the bubbles removed is slowly poured into the container to completely submerge the composite film into the package and then placed in a drying box at 80°C for 4 hours to dry and set. After the solution is completely dry, the piezoelectric nanogenerator is obtained by de-moulding.

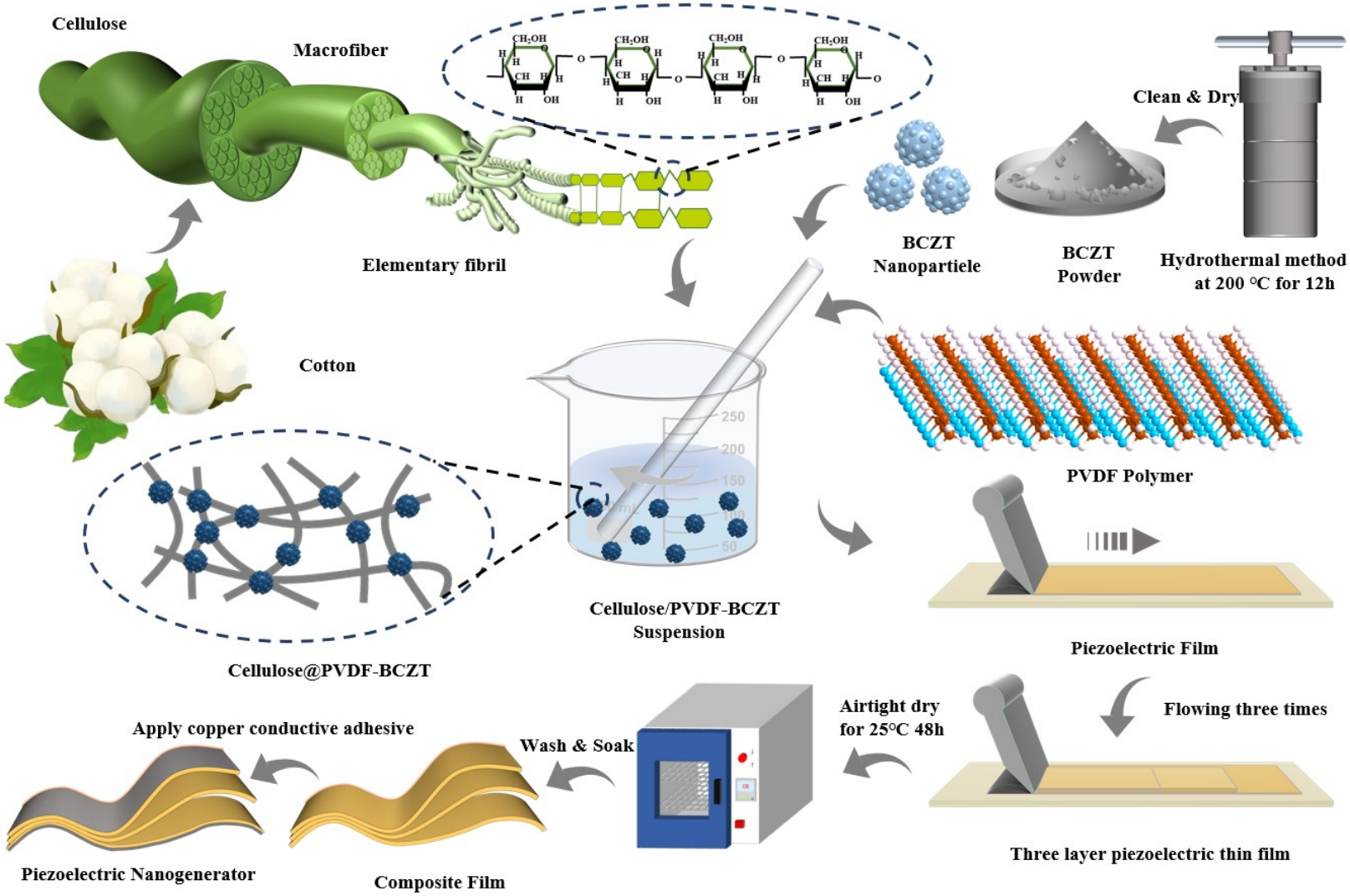

Fig. S1 Experimental technology for preparing C8P2-BCZT piezoelectric nanogenerator

Tab. S1 Lattice parameter of BCZT ceramic fillers obtained from the Rietveld XRD refinement. The R_{wp} and R_p are the weighted profile parameters and unweighted profile parameters, respectively.

	BCZT
a (Å)	4.014
b (Å)	4.014
c (Å)	4.066
c/*a* ratio	1.013
V (Å^3)	65.512
R_p	6.57
R_{wp}	8.78

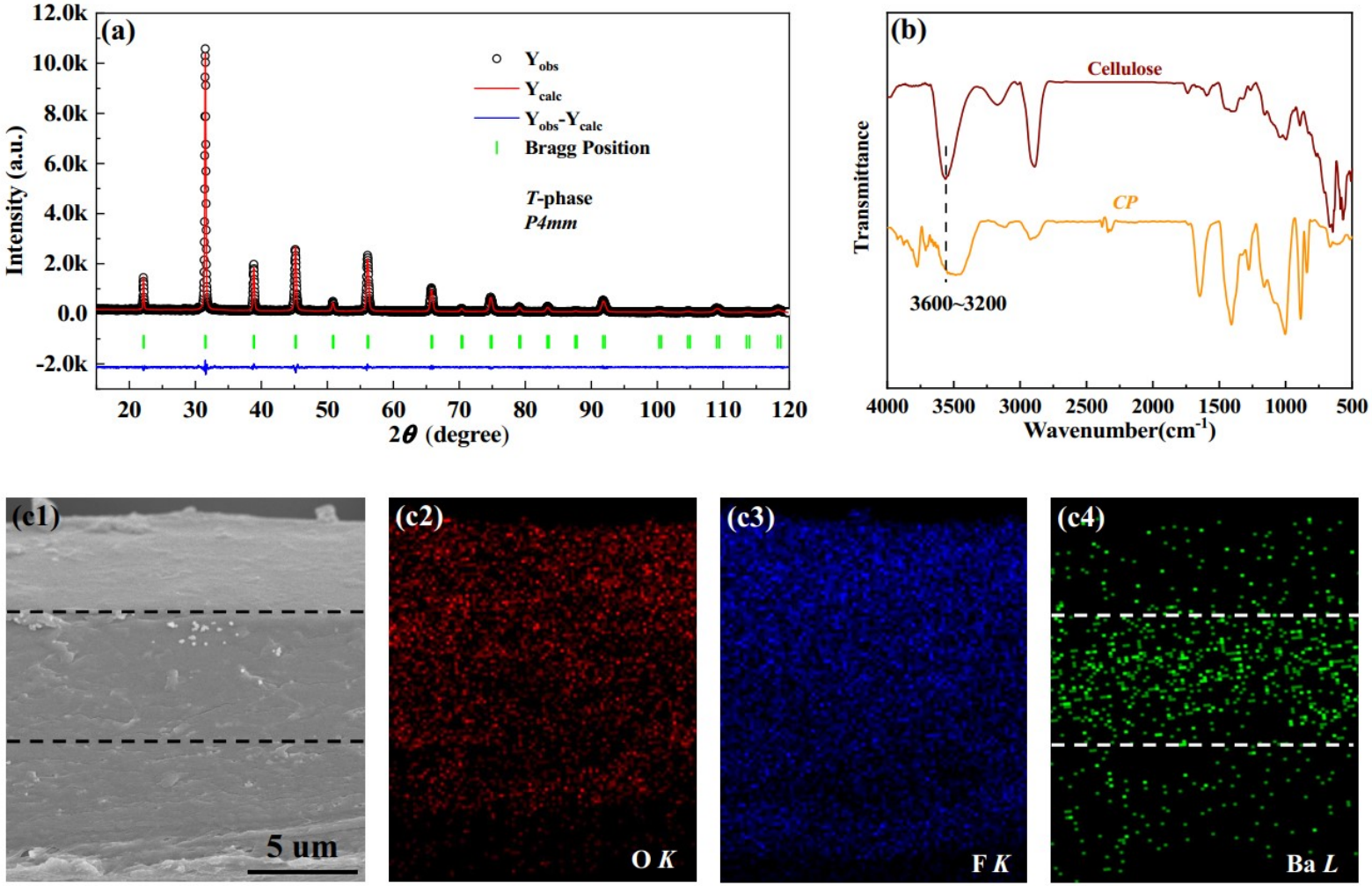

Fig. S2 (a) Rietveld XRD refinement result of BCZT fillers; (b) FT-IR of pristine cellulose and the *CP*; *(c1) SEM cross-sectional of 0-1/3-0; (c2)-(c4) the corresponding EDS mapping for O, F, and Ba.*

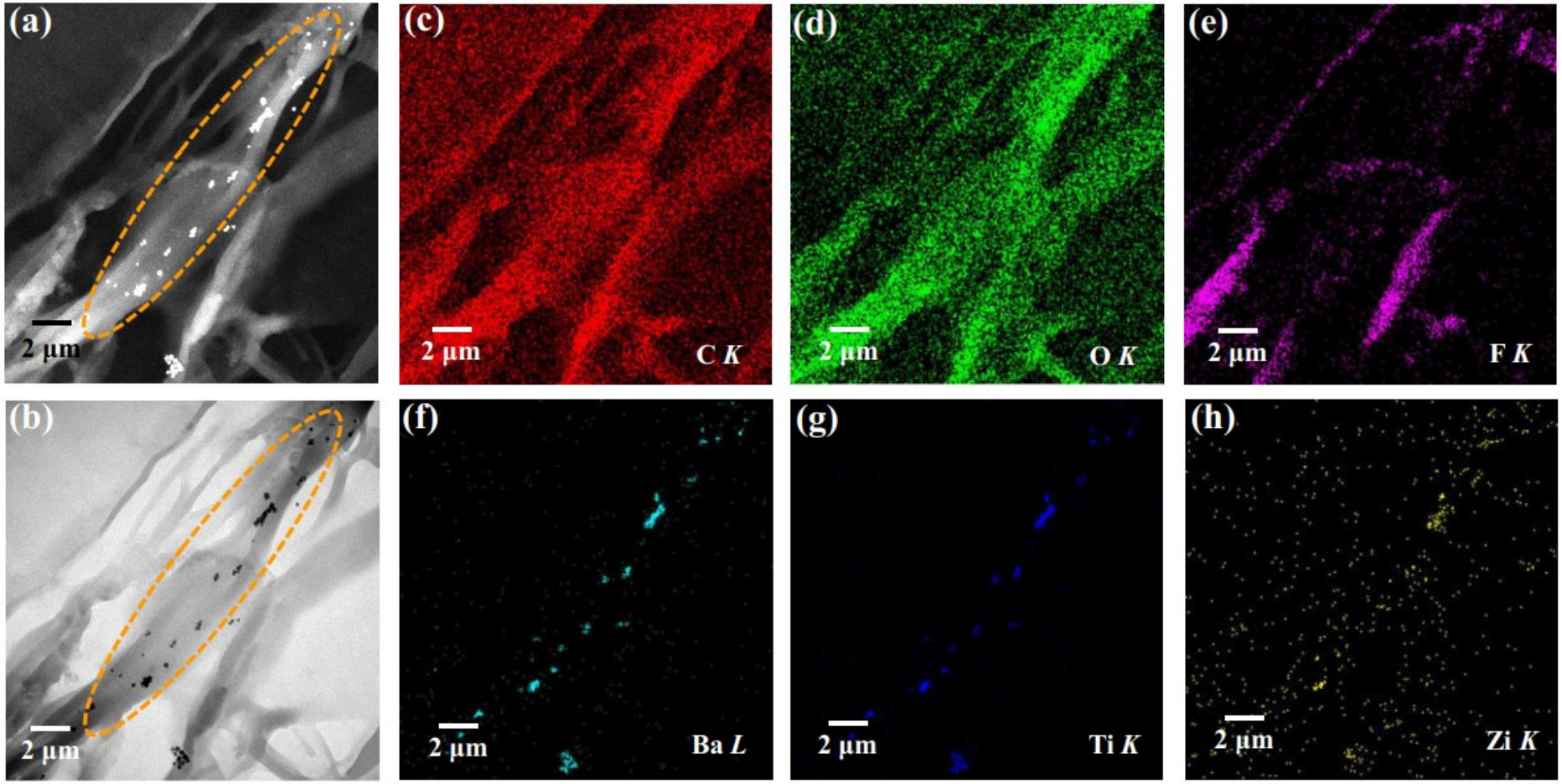

Fig. S3 (a) (b) SEM images of a general area of the inner of the 0-1/3-0 using different detectors; (c)-(h) the corresponding EDS mappings of C, O, F, Ba, Ti, and Zr.

Definition of the Schottky Emission

The Schottky emission in a dielectric device under applied bias is expressed as follows:

$$J=A^{*}T^{2}\exp\left[\frac{-q(\emptyset_S-\sqrt{qE/4\pi\varepsilon_r\varepsilon_0})}{kT}\right]$$

Eq. (S1)

where the J, E, T, ε_r, q, and Φ_S are the current density, electric field, absolute temperature, electron charge, and the Schottky barrier height, respectively; the A^* and ε_0 are the effective Richardson constant and the vacuum permittivity, respectively, which keeps constant. The log$J$ and $E^{0.5}$ should have a linear relation if the conduction mechanism meets the Schottky emission mode.

Explanation of the Formation of the Schottky Barrier

The *C8P2*-BCZT PENG can be seen as three capacitors connected in series, as sketched in Fig. S5(a). The corresponding band diagram can be drawn as Fig. S5(b), and the author will describe the formation of such a band diagram in detail in the following part. Because all of our devices show a symmetrical sandwiched structure, the conditions of the two interfaces between the film and electrode must be the same before and after they come into contact. Therefore, in the following analysis, we only focus on one of them.

(1) Before Contact

According to the previous literature, the work function of Au, PVDF, cellulose, and BCZT is 5.1 eV[2], 5.0 eV[3], lower than 4.58 eV[4], and ~4.8 eV[5], respectively; and the electron affinity of PVDF, cellulose, and BCZT is 3.5~3.9 eV[6,7], 1.62 eV[8], and ~3.9 eV[9], respectively. For simplicity, the band structure of the *CP* matrix and BCZT fillers can be equivalent to a new one in *CP*-BCZT PENG. In this case, the band diagram of *CP* PENG and *CP*-BCZT PENG before the film and electrode contract is illustrated in Fig. S6(a1) and (b1), respectively. Because the work function of BCZT fillers (Φ_{BCZT}) is higher than the work function of both PVDF and cellulose, the equivalent Fermi level of *CP*-BCZT film ($E_{F\text{-}CP\text{-}\mathrm{BCZT}}$) should be lower than the Fermi level of *CP* film ($E_{F\text{-}CP}$), and both $E_{F\text{-}CP\text{-}\mathrm{BCZT}}$ and $E_{F\text{-}CP}$ are lower than the Fermi level of Au (E_{FA}).

(2) After Contact

Considering the majority carriers in the *CP* matrix and BCZT fillers are both electrons[10,11], after the contract, as shown in Fig. S6 (a2) and (b2), the electrons in both configurations transfer from the film side to the electrode side until an equilibrium condition is established, leading to

the electrons' trapped in the interface. The band bending then occurs in both, for the Fermi levels should be aligned. At the same time, a build-in potential, which points from the film side to the electrode side, is formed in both *CP* PENG ($\Phi_{b\text{-}CP}$) and *CP*-BCZT PENG ($\Phi_{b\text{-}CP\text{-}BCZT}$), as well as the depletion layer ($L_{D\text{-}CP}$ and $L_{D\text{-}CP\text{-}BCZT}$). Besides, the Schottky barrier is defined as the difference between the work function of Au (Φ_A) and the electron affinity of *CP* film (χ_{CP}) and *CP*-BCZT film ($\chi_{CP\text{-}BCZT}$) and was written as $\Phi_{s\text{-}CP}$ and $\Phi_{s\text{-}CP\text{-}BCZT}$, respectively. The depletion layer is caused by the electrons' drift, so the width of the depletion layer should have a positive correlation with the electron density in the interface. Due to the inevitable oxygen vacancies in the BCZT lattice, the BCZT fillers exhibit higher electron charge density than the *CP* matrix, so the $L_{D\text{-}CP\text{-}BCZT}$ is broader than the $L_{D\text{-}CP}$. On the other hand, the $\Phi_{s\text{-}CP}$ is higher than the $\Phi_{s\text{-}CP\text{-}BCZT}$. Both the higher Schottky barrier height and the depletion layer thickness positively affect obstructing electron transport.

(3) Forward Bias

As displayed in Fig. S6 (a3) and (b3), when a forward bias (V), which has the same direction as the build-in potential, is applied, the Fermi level of the film moves down, which results in an increment of the build-in potential in both *CP* PENG and *CP*-BCZT PENG. More electrons will be trapped in the interfaces between the film and electrode, so their depletion layers both broaden. The $\Phi_{b\text{-}CP}$ and the $\Phi_{b\text{-}CP\text{-}BCZT}$ in *C8P2* PENG and *C8P2*-BCZT PENG will increase to $\Phi_{b\text{-}CP}+V$ and the $\Phi_{b\text{-}CP\text{-}BCZT}+V$, respectively. Fewer electrons transfer from the electrode to the film and thus result in a lower current and a slower current increase with increasing voltage.

(4) Reserve Bias

As displayed in Fig. S6 (a4) and (b4), when a reserve bias, which has the opposite direction as the build-in potential, is applied, the Fermi level of both the *C8P2* PENG and *C8P2*-BCZT PENG increase, and will be higher than that of the E_{FA}. The $\Phi_{b\text{-}CP}$ and the $\Phi_{b\text{-}CP\text{-BCZT}}$ in *C8P2* PENG and *C8P2*-BCZT PENG will be decreased to $\Phi_{b\text{-}CP}$-V and the $\Phi_{b\text{-}CP\text{-BCZT}}$-$V$, respectively, and the depletion layers in the two configurations will become narrow or even can be ignored. This makes the electrons transfer much easier from the films to the electrode and with applied bias increases, the current increases much faster.

Discussion of the Equivalent Pressure Force in the CP-BCZT PENGs

According to the definition of the piezoelectric equation, which is written as follows:

$$D = d \cdot F \qquad \text{Eq. (S2)}$$

where the D, d, and F are the dielectric displacement, piezoelectric constant, and applied force, respectively, and the dielectric displacement is proportional to the force applied on the piezoelectric material. The relationship between the dielectric displacement and polarization is written as:

$$D = \varepsilon \cdot E + P \qquad \text{Eq. (S3)}$$

in which the P is the piezoelectric polarization, which retained even in the absence of an external electric field. E and ϵ are the electric applied field and the material's dielectric constant, respectively. When combining Eq. (S2) and Eq. (S3), we can have the relationship between the piezoelectric polarization and the force, which can be expressed to be:

$$\varepsilon \cdot E + P = d \cdot F \qquad \text{Eq. (S4)}$$

In our device, the F is composed of two parts: the external force applied on the PENG (F_0) and the inter-force caused by the squeeze between BCZT particles (f_i), so the F is written as:

$$F = F_0 + f_i \qquad \text{Eq. (S5)}$$

The f_i can be expanded as

$$f_i = \chi_1 f_0 + \chi_2 f_0 + \chi_3 f_0 + \ldots \qquad \text{Eq. (S6)}$$

in which the χ_i is the coefficient related to the squeezed degree and is inversely correlated with the inner layer thickness in our work. The f_0 is the unit force applied on each particle and is defined as

$$f_0 = \frac{F_0}{N} \qquad \text{Eq. (S7)}$$

in which the N is the number of the BCZT particle. In our work, all the PENGs suffer F_0, but the f_0 generated in each device is not the same. The *0-1/5-0* owns the highest f_0, and then the *0-1/3-0*, the f_0 in the *0-3/5-0*, is the lowest among the three *CP*-BCZT PENGs. And now the Eq. (S4) can be changed to

$$\varepsilon \cdot E + P = d \cdot F_0 + f_i \qquad \text{Eq. (S8)}$$

One of the recent research reported that the output current of the PENG is directly related to Maxell's displacement current, which can be written as follows:

$$J = \frac{1\partial(S\delta)}{A \quad \partial t} \qquad \text{Eq. (S9)}$$

where the J, A, S, and t are the output current density, cross-section of the device, polarization charge density, and the corresponding boundary surface of the device, respectively[12,13]. Typically, the relationship between polarization charge density and piezoelectric polarization can be written as

$$\delta = \nabla P \qquad \text{Eq. (S10)}$$

For the circumstance of uniform distribution of BCZT fillers, the relationship between the output current density and the applied force can be finally written to be:

$$J = \frac{Sd\ \partial F}{A\varepsilon E\ \partial t} \qquad \text{Eq. (S11)}$$

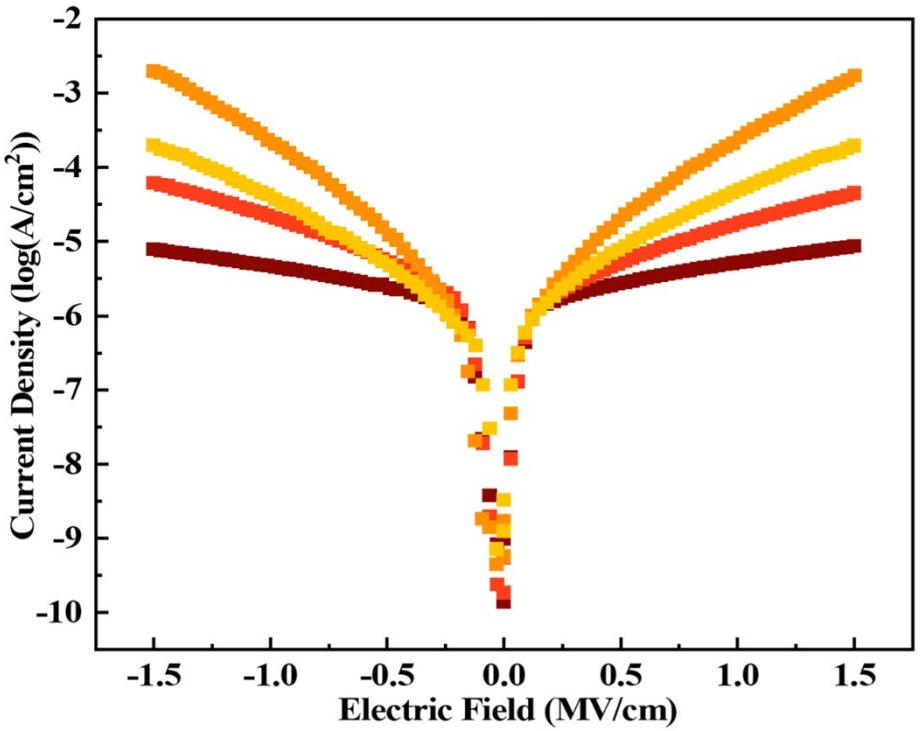

Fig. S4 J-E curves of all the PENGs.

Confirmation of the existence of oxygen vacancies in the BCZT powders

Fig. S5 (c1) and (c2) show the X-ray photoelectron spectroscopy (XPS) spectra for the O 1*s* and Ti 2*p* core levels of the BCZT particles, respectively, and such a measurement was carried out for as-prepared BCZT powders before the composite film fabrication. The peak at ~530.0 eV in Fig. S5 (c1) represents the lattice O, which exists in the oxygen octahedron as sketched in Fig. 2(J), while the peak at ~530.2 eV represents the non-lattice O, which probably comes from the -OH absorbed on the particle surface. It has been well-known that the existence of oxygen vacancies can not be judged by only the XPS spectra for the O[14]. The peaks for Ti 2p3/2 and Ti 2p1/2 in Fig. S5 (c2) can be both fitted out by two peaks, in which the peaks at ~457.8 eV and ~458.2 eV represent the Ti^{3+} 2p3/2 and Ti^{4+} 2p3/2, respectively, while the peaks at ~462.3 eV and ~464.0 eV represent the Ti^{3+} 2p1/2 and Ti^{4+} 2p1/2, respectively. The origin of Ti^{3+} can be explained by the defect equations as follows:

$$O \rightarrow V_O^{\cdot\cdot} + 2e' + \frac{1}{2}O_2 \qquad \text{Eq. (S12)}$$

$$Ti^{4+} + e' \rightarrow Ti^{3+} \qquad \text{Eq. (S13)}$$

The discussions above provide the clue for the formation of the oxygen vacancies in the BCZT lattice to some extent, but in general, some direct evidence, such as the electron paramagnetic resonance(EPR) as shown in Fig. S5 (d), is still needed. The peak at *g*~2.004 reflects the existence of single electrons trapped oxygen vacancies, which proves the Eq. (S12), and the peak at *g*~1.988 reflects the formation of the Ti^{3+} because of the charge unbalance, as explained by Eq. (S13). Such a result agrees well with the conclusion of previous work, thus the existence of the oxygen vacancies in the BCZT powders in our work can be successfully proved[15].

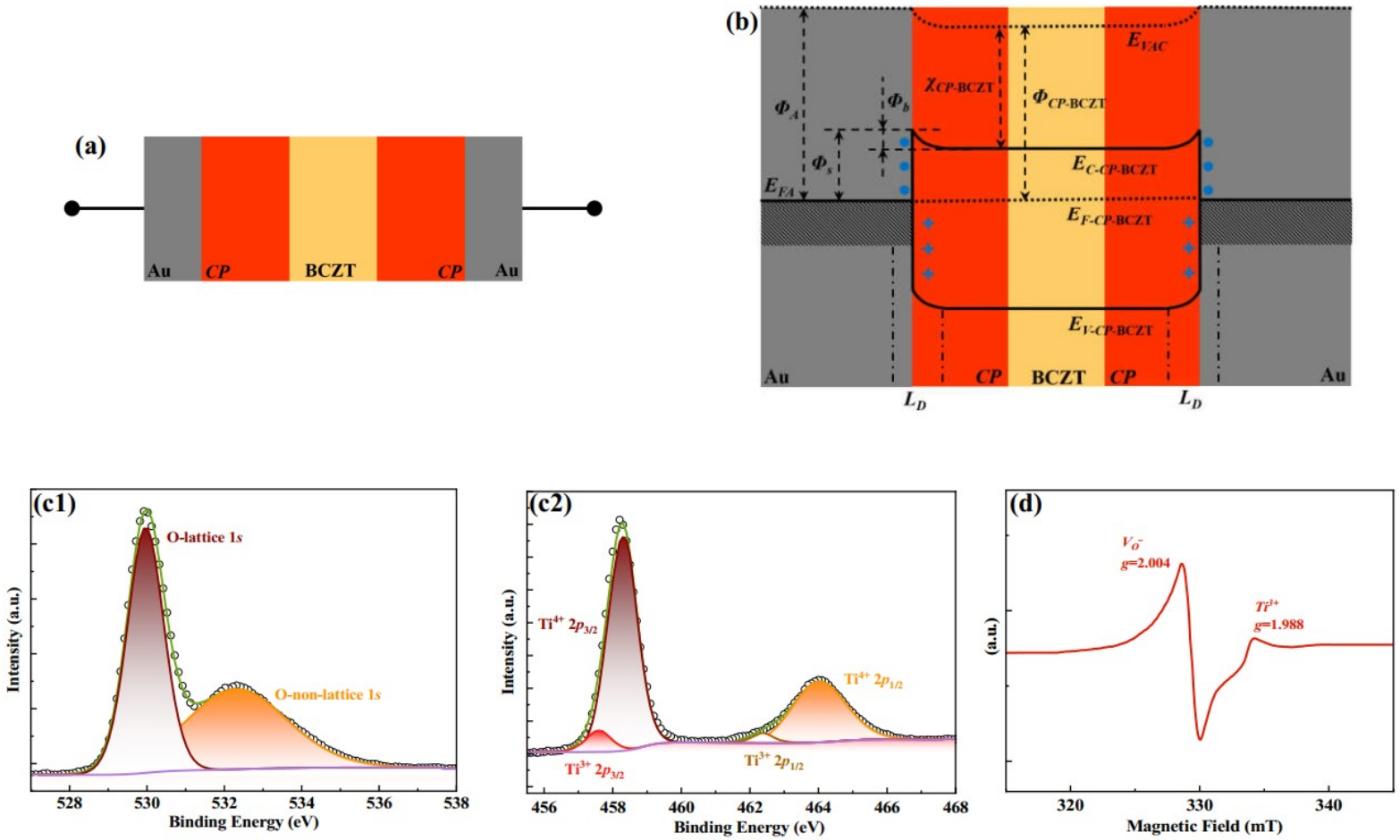

Fig. S5 (a) sketch for the equivalent capacitance of the sandwich structured CP-BCZT PENG; (b) the band diagram to show the band bending of the two Au/CP interfaces in the CP-BCZT PENG structure; XPS spectra for (c1) O 1s core level of the BCZT particles; (c2) Ti 2p core level of the BCZT particles; (d) EPR spectra of

the BCZT particles

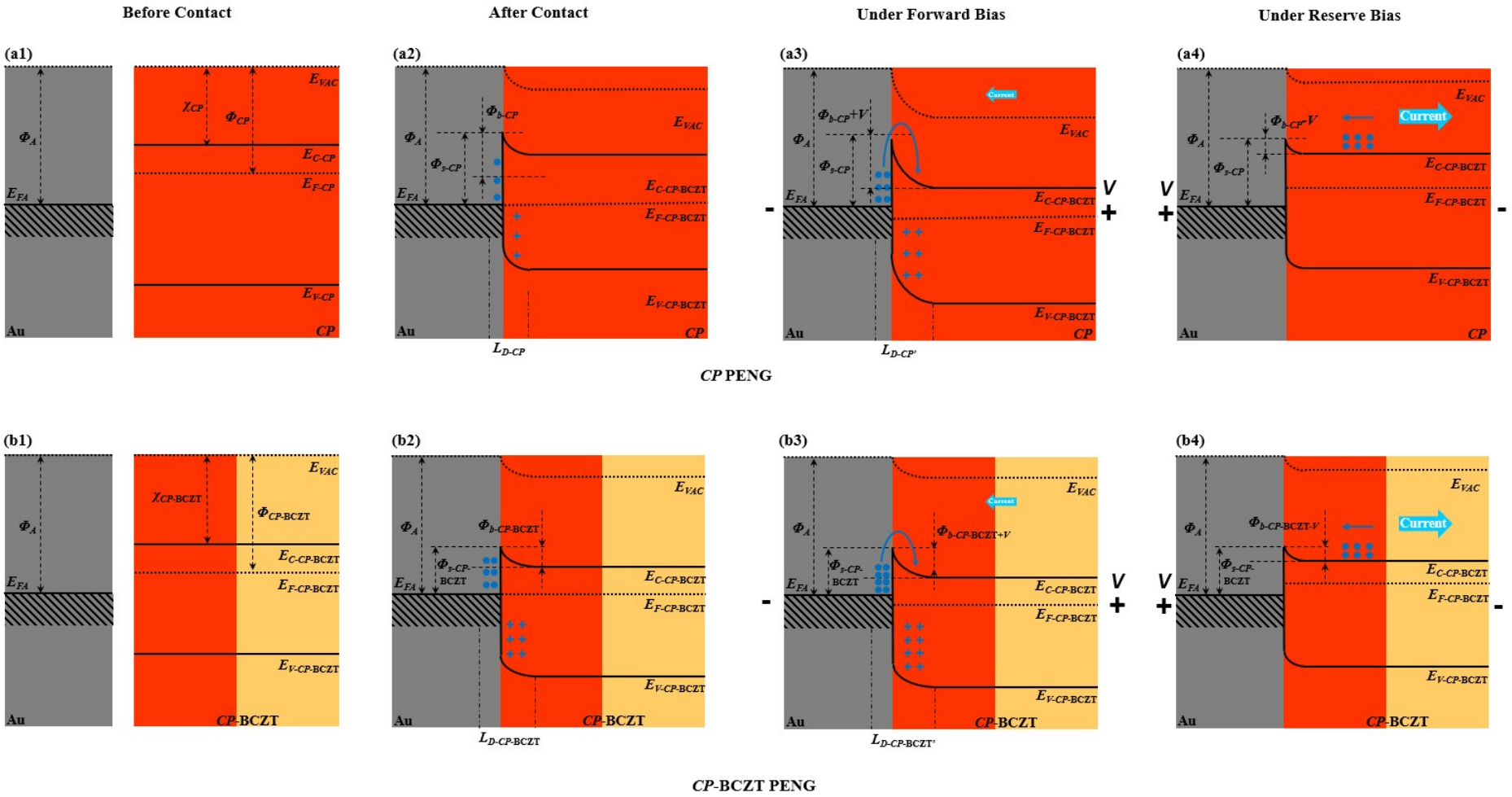

Fig. S6 band diagram of (a1) Au/CP interface; (b1) Au/CP interface before contact; band diagram of (a2) Au/CP interface; (b2) Au/CP interface after contact; band diagram of (a3) Au/CP interface; (b3) Au/CP interface under forward bias; band diagram of (a4) Au/CP interface; (b43) Au/CP interface under reserve bias.

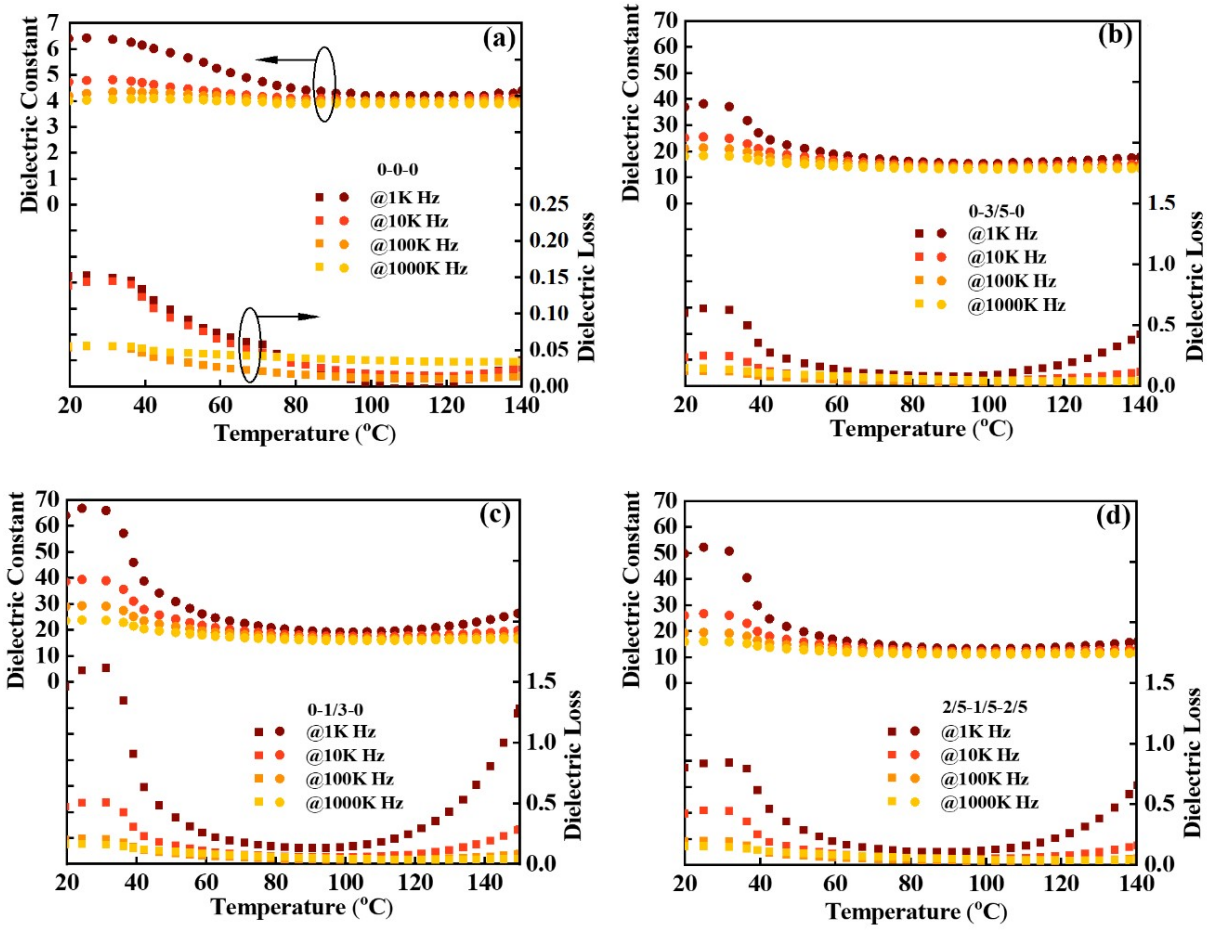

Fig. S7 temperature dependence of dielectric constant (ε) and dielectric loss (tan δ) of all the PENGs.

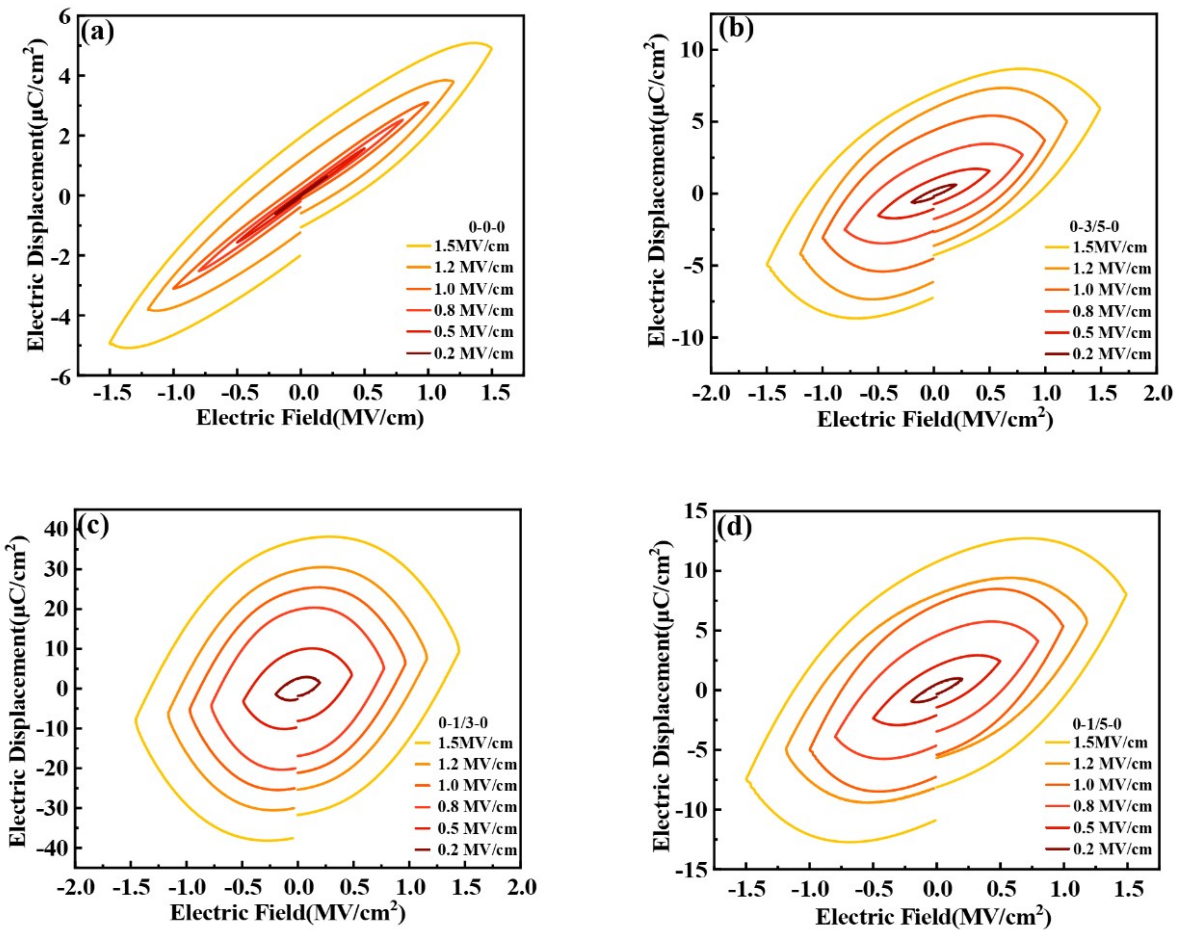

Fig. S8 P-E loops of all the PENGs.

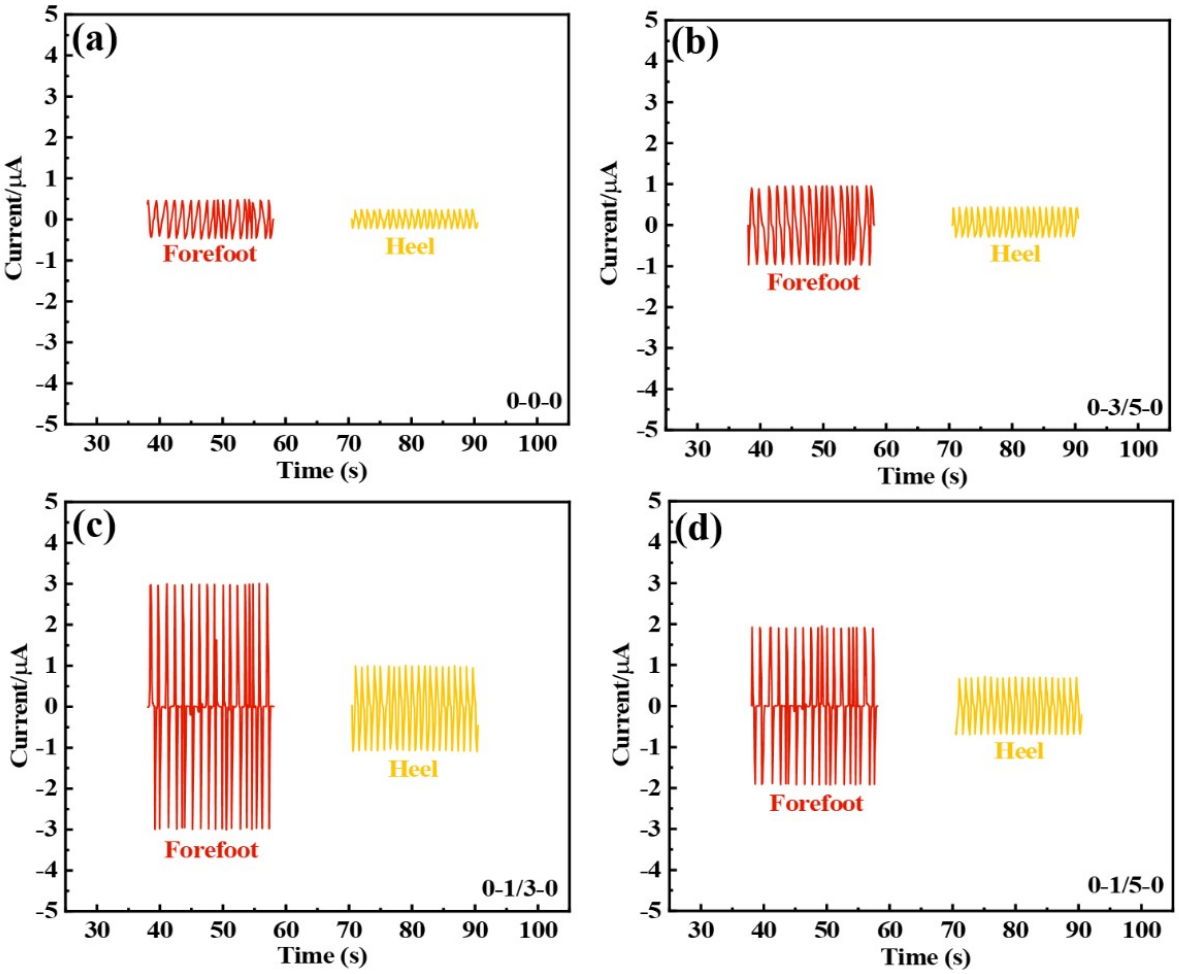

Fig. S9 I_S of all the PENGs generated at different sole positions.

References

1. S. Zhang, J. Liu, Q. Guo, N. Wei, Y. Ning, Y. Bai, Y. Tian, T. Wang, Z. Sun, Y. Pu, *Composites Part A: Applied Science and Manufacturing*, 2023, **165**, 107329.
2. B. Ofuonye, J. Lee, M. Yan, C. Sun, J. M. Zuo, and I. Adesida, *Semicond. Sci. Technol.*, 2014, **29**(9), 095005.
3. S. Kim, Y. Song, and M. J. Heller, *J. Nanomater.*, 2017.
4. Y. Shao, C. P. Feng, B. W. Deng, B. Yin, and M. B. Yang, *Nano Energy*, 2019,**62**, 620-627.
5. T. Schulmeyer, S. A. Paniagua, P. A. Veneman, S. C. Jones, P. J. Hotchkiss, A. Mudalige, and N. R. Armstrong, *J. Mater. Chem.*, 2017, **17**(43), 4563-4570.
6. R. Chikkonda, A. Ravindran, S. Saikia, A. R. T. Sathyanathan, A. Chelvane, A. Subramanian, J. R. K. Chinnayya, R. B. Gangineni, *J. Appl. Polym. Sci*., 2021, **138**, 50018.
7. M. Kumar, D. G. Georgiadou, A. Seitkhan, K. Loganathan, E. Yengel, H. Faber, D. Naphade, A. Basu, T. D. Anthopoulos, K. Asadi, *Adv. Electron. Mater*., 2020, **6**, 1901091.
8. R. Pontoh, V. E. Rarisavitri, C. C. Yang, M. F. Pura, D. S. B. Anugrah, *Indones. J. Chem*., 2022, **22**, 253-262.
9. M. Vagadia, A. Ravalia, P. S. Solanki, P. Pandey, K. Asokan, and D. G. Kuberkar, *AIP Adv*., 2014 **4**(5).
10. A. Laudari, J. Barron, A. Pickett, and S. Guha, *ACS Appl. Mater. Interfaces*, 2020, **12**(24), 26757-26775.
11. J. Nowotny, and M. Rekas, *Solid State Ionics*, 1991 **49**, 135-154.
12. L. Gu, J. Liu, N. Cui, Q. Xu, T. Du, L. Zhang, and Y. Qin, *Nat. Commun.*, 2020 **11**(1),

1030.

13. Z. L. Wang, *Mater. Today*, 2017, **20**(2), 74-82.

14. T. J. Frankcombe, Y. Liu, Chem. Mater. 2023, **35**(14) 5468–5474.

15. G. J. Wang, J. Zheng, H. Bi, S. T. Wang, J. Wang, J. Sun, Y. F. Guo, C. C. Wang, Scripta Mater. 2019, **162** 28-32.